Journal of Non Crystalline Solids. Vol. 355. Núm. 2. 2009. Pag. 109-113
http://dx.doi.org/10.1016/j.jnoncrysol.2008.10.017

Preferential Co partitioning to α-Fe in nanocrystalline CoFeNbB alloys by Mn addition.

M. Millán[a], J.S. Blázquez[a], C.F. Conde[a], A. Conde[a]*, S. Lozano-Pérez[b], P. Ochin[c]

[a] *Dpto. Física de la Materia Condensada, ICMSE-Univ. Sevilla, P.O.Box 1065, Sevilla 41080, Spain.*

[b] *Department of Materials, University of Oxford, Parks Road, Oxford, OX1 3PH, UK.*

[c] *CNRS-Université Paris XII, Institute of Chemistry and Materials Paris-Est ICMPE, 2-8 Rue Henri Dunant 94320, Thiais, France.*

ABSTRACT

Influence of Mn addition on the microstructure and hyperfine parameters of amorphous and nanocrystalline $Co_{60}(FeMn)_{18}Nb_6B_{16}$ alloys has been studied. Although Mn addition does not yield significant differences in crystallization kinetics and in the phases formed after each transformation, it seriously affects the partitioning of Co during nanocrystallization. Whereas for Mn free alloy Co is homogeneously distributed throughout the amorphous matrix and the nanocrystals, in Mn containing alloy Co is enriched in the α-FeCo nanocrystals. This fact prevents the exhaustion in Fe of the amorphous matrix and the crystalline volume fraction achieved at the end of nanocrystallization in the case of Mn containing alloy is ~20 % higher than in the Mn free alloy.

*Corresponding author: Prof. A. Conde

Departamento de Física de la Materia Condensada. Universidad de Sevilla.

Apartado 1065, 41080 Sevilla (Spain).

Phone: (34) 95 455 28 85

Fax: (34) 95 461 20 97

Journal of Non Crystalline Solids. Vol. 355. Núm. 2. 2009. Pag. 109-113
http://dx.doi.org/10.1016/j.jnoncrysol.2008.10.017

1 Introduction

Soft magnetic nanocrystalline alloys are subject of research interest since the discovery of FINEMET composition in 1988 [1]. Since then, a huge number of compositional variations have been proposed in order to enhance the soft magnetic properties and to explore the nanocrystallization phenomena and the resulting microstructure [2,3]. Both aims are interrelated as the microstructure, characterized by nanosized ferromagnetic crystallites embedded in an amorphous ferromagnetic matrix, is the responsible for the outstanding soft magnetic properties observed in these alloys due to an averaging out of the magnetocrystalline anisotropy and a reduced value of magnetostriction as demonstrated by the two phase anisotropy model [4]. In this frame, the control of grain size and crystalline volume fraction is a very important task in order to optimize the properties of the system.

The general composition of nanocrystalline alloys is LT-ET-M-(Cu). LT is a late transition metal, which is the main component of the system (70-90 at. %) and will form the nanocrystals. LT is generally Fe as the magnetocrystalline anisotropy of bcc Fe phase is smaller than those of fcc and hexagonal systems. However, the partial substitution of Co for Fe presents the advantage of a higher Curie temperature for both amorphous matrix and bcc Fe(Co) phase (the latter being the stable phase for the binary Fe-Co system up to a high concentration of Co, >75 at. %). ET is an early transition metal (Zr, Nb, Hf, etc.) which, due to its very low solubility in the FeCo nanocrystals and slow difussivity in the amorphous matrix, is expelled out from the crystalline regions to the matrix. Therefore, Nb piles up at the crystal edges and constrains their growth to a nanometric scale. M is a metalloid (B, Si, P, etc) which is used to enhance the glass forming ability of the liquid system, in order to obtain a precursor amorphous alloy from which the nanocrystalline system will be produced after partial controlled crystallization. The addition of Cu is not always necessary to produce a nanocrystalline microstructure by partial devitrification but it can refine the final microstructure in some compositions where Cu clustering phenomenon occurs previous to the nanocrystallization onset [5]. Similar refinement can be also obtained in $Co_{60}Fe_{18}Nb_6B_{16}$ alloys [6], but the high Co content yields a restricted crystallization process due to exhaustion of Fe in the amorphous matrix [7]. This exhaustion is a

consequence of the homogeneous Co distribution throughout the amorphous matrix and the nanocrystals [8], also observed for other Co containing systems [9]. In this work, the frustrated crystallization process is overcome by the addition of a small amount of Mn (4 at. %). The crystallization processes of both systems Mn free and Mn containing alloys are compared.

2 Experimental

Ribbons 10 mm wide and about 20 μm thick with nominal compositions $Co_{60}Fe_{18-x}Mn_xNb_6B_{16}$ (x=0 and 4) were prepared by planar flow casting in argon atmosphere. Chemical composition of the alloys was checked by inductionally coupled plasma spectroscopy and energy dispersive X-ray spectroscopy (EDX). Differential scanning calorimetry (DSC) was performed in a Perkin-Elmer DSC-7 (temperature error $\Delta T=\pm 1$ K) and thermomagnetic gravimetry (TMG) in a Perkin-Elmer TGA-7 ($\Delta T=\pm 1$ K) both under argon atmosphere. In the last technique, the magnetic field of a small magnet (~20 mT) is applied and changes in the magnetic force acting upon the sample, related to the variations in magnetization with temperature, are recorded as apparent weight changes of the sample.

The microstructure was studied at room temperature by X-ray diffraction (XRD) using Cu-Kα radiation, transmission electron microscopy (TEM) in two microscopes: a Philips CM200 and a CM20 operated at 200 kV and by Mössbauer spectrometry. Mössbauer spectra were recorded at room temperature in a transmission geometry using a $^{57}Co(Rh)$ source. The incident γ-beam was set perpendicular to the ribbon plane. The values of the hyperfine parameters were obtained by fitting with NORMOS program [10] and the isomer shift, *I*, was quoted relative to an α-Fe foil at 300 K. In all the studied cases, the quadrupolar splitting was negligible.

3 Results

Figure 1 shows DSC scans at 10 K/min of as-cast samples of the two studied alloys. The devitrification occurs in three different stages but, for the Mn free alloy, the third transformation

stage is only observed below 1000 K for heating rates $\beta \leq 5$ K/min [11]. Table 1 shows the relevant temperatures of the crystallization processes in the studied alloys. Although there are no significant differences between the crystallization onset temperatures, T_O, in the two studied alloys, the peak temperature, T_P, of the first exothermic event for the Mn containing alloy shifts to higher values with respect to that of the Mn free alloy. On the other hand, T_P of the second and third transformation processes decreases with the addition of Mn. Therefore, the addition of 4 at.% Mn yields a decrease of the thermal stability of the nanocrystalline microstructure developed in these alloys.

Figure 2 shows TMG plots at 40 K/min of the as-cast samples. The magnetization does not fall to zero in the studied thermal range, indicating that the Curie temperature, T_C, of the amorphous sample is above the crystallization onset temperature. Thus, a decrease of the magnetization is observed from room temperature up to ~750 K followed by a magnetization increase between 750-900 K due to the crystallization of α-Fe(Co,Mn) nanocrystals with a higher T_C. The overlapping between the decrease in magnetization due to the approach to T_C of the amorphous phase and its rise due to the formation of nanocrystals prevents a precise measurement of both the Curie temperature of the amorphous phase ($T_C^{Am} >$ ~750 K) and the crystallization onset temperature by this technique. However, it is clear that T_C of the amorphous phase decreases in the Mn containing alloy with respect to the Mn free alloy.

At higher temperatures (coincident with that of the corresponding second exothermic process detected by DSC), magnetization sharply decreases for the studied alloys due to a recrystallization phenomenon, causing part of the already formed nanocrystals and the residual amorphous matrix, to form fcc $Fe_{23}B_6$ type phase [12]. At even higher temperatures (>1000 K), a smoother decrease of magnetization is observed due to the approach to T_C of the α-Fe(Co) nanocrystals. In fact, T_C for α-$Fe_{1-y}Co_y$ crystals with y>0.2 is above its α-γ structural transition (~1200 K) [13]. This smooth decrease in magnetization above 1000 K is not clearly observed for the Mn free alloy, indicating a higher Curie point (not achievable due to the α-γ transition) for the crystalline phases present in this alloy after the third crystallization event.

Journal of Non Crystalline Solids. Vol. 355. Núm. 2. 2009. Pag. 109-113
http://dx.doi.org/10.1016/j.jnoncrysol.2008.10.017

Figure 3 shows the XRD patterns of the 4 at. % Mn containing alloy after different heat treatment conditions (see table 2). Results confirm the formation of a nanocrystalline microstructure during the first exothermic process detected by DSC and, after the second transformation stage, bcc α-Fe(Co) and fcc $(FeCoMnNb)_{23}B_6$ are the main phases detected.

The lattice parameter of the α-Fe(Co) phase decreases with Mn addition, being 2.846 and 2.838± 0.002 Å for 0 and 4 at. % of Mn, respectively. Neglecting the effect of Mn on the lattice parameter of bcc Fe [14], these values would lead to a Co content in the crystalline phase ~60 and ~70 % [15] for 0 and 4 at. % of Mn in the alloy, respectively, i.e. close to the compositional limit of the α-Fe(Co) phase [13]. In the case of Mn-free alloy, the Co content in the crystallites was measured as 60 % using three dimensional atom probe [8] in agreement with its higher value of lattice parameter.

The crystalline volume fraction can be estimated using a deconvolution procedure, detailed elsewhere [7], as the area ratio between the crystalline (110) peak and the total area of the diffraction maximum including the amorphous contribution and taking into account the different scattering factors of the elements present in the alloy. In order to do so, it would be necessary to know the composition of the crystalline phase but this problem can be overtaken as the only elements suitable to be in α-Fe grains are Fe, Co and Mn, which have very similar scattering factors. It is worth mentioning that the crystalline fraction at the final stages of nanocrystallization is clearly higher for the Mn containing alloy (X_C^F =55 %) than for Mn free alloy (X_C^F =43 %). This low value of X_C^F was explained by exhaustion of the amorphous matrix in Fe content in the Mn-free alloy. The composition of the nanocrystals is $Fe_{40}Co_{60}$ for this alloy, being the Co concentration the same throughout the amorphous and crystalline phases. However, the higher crystalline fraction observed for the Mn containing alloy is similar to the values found in alloys with similar composition but with lower Co content [7,16,17]. This will require a lower Fe concentration in the crystalline phase, $C_{Fe}^{Cryst} \leq 25$ at. %, than that of the Mn

free alloy, C_{Fe}^{Cryst} = 40 at. %, in order to avoid a fictitious negative Fe concentration in the amorphous matrix. The consequent requirement of higher concentration of Co in the crystalline phase would be in agreement with the tendency observed in the lattice parameter. The presence of Mn in nanocrystals cannot be discarded for the alloy with 4 at. % of Mn, as it can be dissolved in α-Fe phase up to ~3 at. % [13].

TEM images of nanocrystalline samples agree with the description obtained from XRD results. Figure 4 shows bright field images of both studied alloys heated up to the final stages of the nanocrystallization process (R4 in table 2). Crystal size distributions are also shown in this figure. The achieved nanocrystalline microstructure is very similar for the alloys, exhibiting an average value of the crystal size <D>= 4.4 and 4.7 ± 0.1 nm for 0 and 4 at. % of Mn, respectively.

Figure 5 shows the spectra of the studied alloys at different stages of devitrification. The spectra of amorphous samples were fitted using a distribution of hyperfine magnetic fields, DHF. In the case of nanocrystalline samples, a set of discrete values of hyperfine fields, H_{hyp}, and two DHFs were used to fit the experimental data. The two DHFs would roughly correspond to the amorphous phase and to the interface amorphous-nanocrystal region, respectively. The distinction between the limits of hyperfine magnetic field contributions corresponding to the amorphous matrix or to the interface region is ambiguous and, therefore, overlapping between them was allowed in the fitting process. The main reason for using two different DHFs is to allow non-correlated isomer shift values for high and low hyperfine magnetic fields in attention to their possible different nature. In this paper, results will be given as the average between these two contributions: amorphous+interface (A+I) contribution.

4 Discussion

Kinetics of non isothermal crystallization can be studied applying the Kissinger method [18] (activation energies, Q, are shown in table 3), indicating that Q increases with Mn addition. Local Avrami exponent, n(X) was obtained from a non-isothermal approach developed for

isokinetic processes [19]. Results show that nanocrystallization kinetics is very slow for the studied samples (n<1) and becomes even slower as the nanocrystallization progresses. These very low values of Avrami exponent have been recently explained in the frame of an instantaneous growth process [20].

Figure 6 shows the hyperfine magnetic field distributions obtained for the studied alloys as a function of the annealing temperature. Amorphous samples exhibit a bimodal character of the hyperfine field distribution characterized by two different peaks, one at low fields, ascribed to Fe atoms in poor Fe/Co environments (centred at ~11 T for the Mn containing alloy and at 12 T for the Mn free alloy, respectively), and a second peak at higher values, ascribed to Fe atoms at Fe/Co rich environments, (at 26.0 and 25.0 T for 0 and 4 at. % of Mn containing alloys, respectively). The estimated fraction of the smallest peak (centred at 11-12 T) is about 6 and 8 % in as-cast state and decreases after structural relaxation to 4 and 6 % for 0 and 4 at. % of Mn alloys, respectively. The H_{hyp} values corresponding to this peak have been assigned to Fe atoms with 4 Nb atoms as near neighbours in bcc supersaturated solutions [21]. Although the Fe environment in amorphous systems may differ with respect to bcc environment, it would be possible to assign a higher number of Nb atoms to the average Fe neighbourhood in 4 at. % Mn containing alloy. Structural relaxation leads to a decrease of the average number of Nb neighbors in the vicinity of Fe for both studied alloys.

As nanocrystallization progresses, the discrete H_{hyp} contributions ascribed to crystalline sites appear. For nanocrystalline samples, the A+I contribution indicates the amorphous plus interface contribution, i. e. the addition of the two used DHFs. In the case of the fully crystallized samples, this contribution takes into account those phases containing Fe but different to α-FeCo (mainly $Fe_{23}B_6$ type phase). The average hyperfine parameters of the α-FeCo nanocrystals are similar for the two compositions ($\langle H_{hyp} \rangle^C$ ~33.6 T and $\langle I \rangle^C$ ~0.02 mm/s). This fact is apparently in contradiction with the XRD results, from which a higher Co content in the crystalline phase is inferred for the Mn containing alloy. However, the value of the average hyperfine magnetic field in α-Fe(Co) is not only determined by the Co content but also by the presence of the ordered α' phase [22,23]. This phase, which compositional range

extents up to >70 at. % of Co [13], leads to a decrease of $<H_{hyp}>$ with respect to the fully disordered phase [22]. Moreover, the possible presence of Mn into the nanocrystals for the alloy containing this element cannot be discarded as commented above.

Combining XRD and Mössbauer results it is possible to extract some information from the nanocrystalline phase. As known, crystalline volume fraction obtained from XRD can be approximated to the fraction of the total atoms of the alloy in the crystalline phase, whereas, the area fraction of the discrete sextets needed to fit the Mössbauer spectra indicates the fraction of Fe atoms which are in pure crystalline sites. This means that the atoms at the interface region are not taken into account. Although this region belongs to the crystalline phase, the vicinity of enriched Nb regions at the edge of the nanocrystals affects the hyperfine magnetic field of Fe atoms in this region. Considering that the very low crystalline volume fraction achieved in the Mn free alloy at the end of the nanocrystallization is due to exhaustion of Fe in the matrix, it is possible to estimate the size of the interface region once the average size of the nanocrystals is known from TEM. The total fraction of Fe atoms at the crystalline phase is:

$A_{Total}^{Cryst} = A_{Core}^{Cryst} + A_{Int}^{Cryst}$, where A_{Core}^{Cryst} is the fraction of Fe atoms at the core of the nanocrystals (not affected by atoms outside the nanocrystals) and A_{Int}^{Cryst} is the fraction of Fe atoms at the interface. The ratio $\frac{A_{Core}^{Cryst}}{A_{Total}^{Cryst}} = \left(\frac{D - 2\delta}{D} \right)^3$ depends on the size of the nanocrystals, D, and on the thickness of the interface region, δ. As the matrix is exhausted in Fe, the Fe fraction at the end of the nanocrystallization contributing to the discrete sextet, A_{Core}^{Cryst}=0.58, yields a value of the interface thickness, δ=0.4 nm, similar to that found for other systems [21]. Using this value of δ for the Mn containing alloy, it is possible to estimate the total fraction of Fe atoms at the crystalline phase as A_{Total}^{Cryst} = 0.79. Taking into account the crystalline volume fraction obtained from XRD, the Fe content in the crystalline phase at the end of the nanocrystallization should be ~20 % for 4 at. % Mn containing alloy.

Journal of Non Crystalline Solids. Vol. 355. Núm. 2. 2009. Pag. 109-113
http://dx.doi.org/10.1016/j.jnoncrysol.2008.10.017

The second transformation stage detected by DSC corresponds to a recrystallization phenomenon, as it was previously demonstrated for Mn-free alloys [12]. The resulting microstructure is mainly formed by nanocrystals (~10 nm in size) of α-Fe(Co) phase and large crystals of $(FeCoMnNb)_{23}B_6$ phase. As an example, figure 7 shows a TEM bright field image of the alloy with 4 at. % of Mn heated up to the peak temperature of the second transformation event (R5 in table 2). A selected area diffraction pattern and a convergent beam electron diffraction pattern are also shown. The former shows diffraction rings ascribed to bcc α-FeCo nanocrystals and spots which may be ascribed to the large crystals of fcc $Fe_{23}B_6$ type phase, the latter shows a [110] zone axis diffraction pattern corresponding to a $Fe_{23}B_6$ type crystal (the darkest crystal at the center of the bright field image). It is worth mentioning that this phase is not clearly observed on XRD patterns but some tiny traces (see figure 3) could be indexed as maxima of a $Fe_{23}B_6$ type phase, supported by TEM results.

The recrystallization phenomenon is evident from the sharp decrease in magnetization detected by TMG (see figure 2) at the temperature of the second transformation stage observed by DSC. However, the fraction of Fe atoms in pure crystalline sites (excluding interface region) from Mössbauer results decreases for the Mn free alloy, whereas it still increases for Mn containing alloy after this transformation. This may be affected by the increase in the size of the α-FeCo nanocrystals. For a constant amount of this phase, a change from 4.5 to 10 nm would lead to an increase of A_{Core}^{Cryst} from 0.5 to 0.7. Therefore, a larger final nanocrystal size would justify an increase in A_{Core}^{Cryst} even if the fraction of α-Fe(Co) phase decreases. An enrichment in Fe of this phase during the second transformation stage could also support the data.

Conclusions

The main conclusions derived from this work on the effect of Mn addition on the microstructure and magnetic properties of high Co content FeCoNbB amorphous and nanocrystalline alloys are listed below:

- The crystalline volume fraction achieved at the end of the nanocrystallization process is significantly affected by Mn addition, being smaller for Mn free alloy than for Mn containing alloy. For the former alloy, nanocrystallization ends due to exhaustion in Fe of the amorphous matrix as the nanocrystals are only enriched in Fe. However, for the latter alloy, nanocrystals are enriched in both Fe and Co and the final crystalline volume fraction is similar to that observed for alloys where the matrix is still rich in Fe at the end of the nanocrystllization.
- The composition of the crystalline phase in Mn containing alloy could be estimated by combining X-ray diffraction and Mössbauer results as approximately $(FeMn)_{25}Co_{75}$, close to the maximum Co concentration in α-Fe type phase in the binary phase diagram.

Acknowledgements

Work supported by MEC of the Spanish Government and EU FEDER (Project MAT2007-65227) and the PAI of the Regional Government of Andalucía (Project P06-FQM-01823). The TEM investigations were partially supported by the IP3 project of the 6th Framework Programme of the European Commission: ESTEEM Contract number 026019. J.S.B. acknowledges a research contract from Junta de Andalucía.

Journal of Non Crystalline Solids. Vol. 355. Núm. 2. 2009. Pag. 109-113
http://dx.doi.org/10.1016/j.jnoncrysol.2008.10.017

Table 1. Onset and peak temperatures from DSC records taken at 10 K/min.

Mn content (at. %)	T_O (K)	T_{P1} (K)	T_{P2} (K)	T_{P3} (K)
0	731	748	907	--
4	734	759	893	979

Table 2. Treatment temperatures of the different studied samples.

Mn content (at. %)	Temperature of treatment (K)					
	R0	R1	R2	R3	R4	R5
0	As-cast	644	739	759	794	909
4	As-cast	650	745	765	800	893

Table 3. Activation energies of the different thermal transformations.

Mn content (at. %)	1st Peak (eV)	2nd Peak (eV)	3rd Peak (eV)
0	3.5	4.6	--
4	4.1	5.1	~6

Journal of Non Crystalline Solids. Vol. 355. Núm. 2. 2009. Pag. 109-113
http://dx.doi.org/10.1016/j.jnoncrysol.2008.10.017

Figure captions

Figure 1. DSC plots of as-cast samples at 10 K/min.

Figure 2. TMG plots of as-cast samples at 40 K/min

Figure 3. XRD patterns of Mn containing alloy after heating up to different temperatures (see table 2)

Figure 4. Bright field TEM images and crystal size distributions of R4 samples (see table 2) of both alloys.

Figure 5. Mössbauer spectra of the different studied samples.

Figure 6. Hyperfine magnetic field distribution of the different studied samples.

Figure 7. Bright field TEM image (left), selected area diffraction pattern (right and above) and convergent electron beam diffraction pattern of a fcc $(FeCoMnNb)_{23}B_6$ crystal (right and below) of R5 sample (see table 2) of the Mn containing alloy.

Journal of Non Crystalline Solids. Vol. 355. Núm. 2. 2009. Pag. 109-113
http://dx.doi.org/10.1016/j.jnoncrysol.2008.10.017

Figure 1

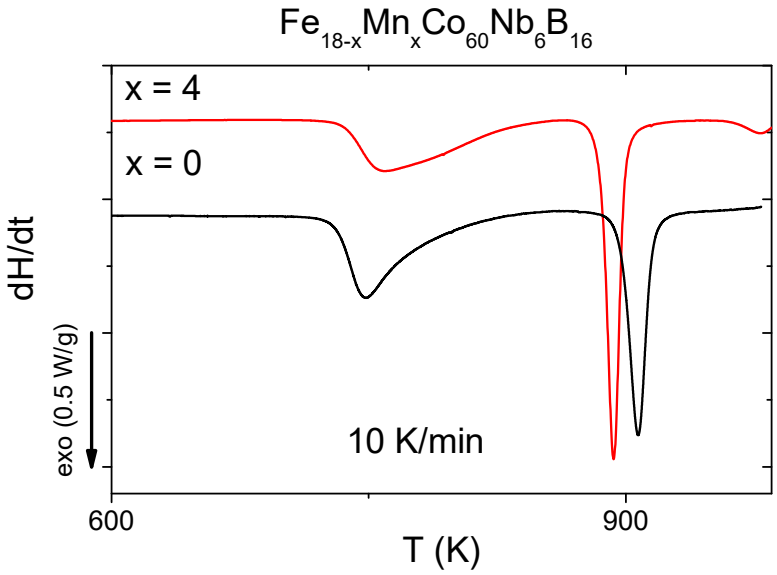

Journal of Non Crystalline Solids. Vol. 355. Núm. 2. 2009. Pag. 109-113
http://dx.doi.org/10.1016/j.jnoncrysol.2008.10.017

Figure 2

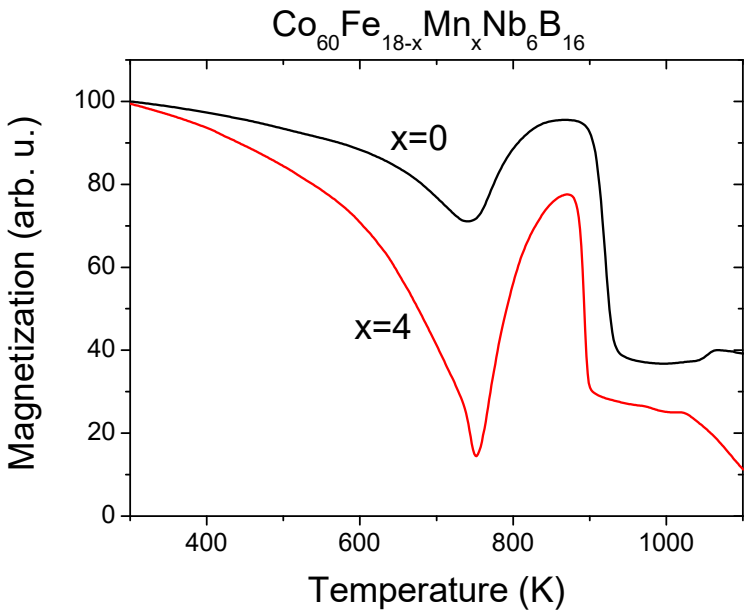

Journal of Non Crystalline Solids. Vol. 355. Núm. 2. 2009. Pag. 109-113
http://dx.doi.org/10.1016/j.jnoncrysol.2008.10.017

Figure 3

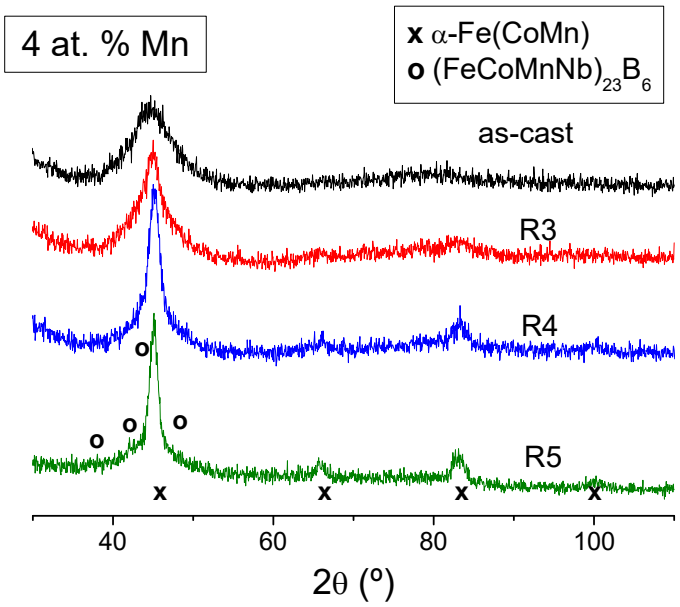

Journal of Non Crystalline Solids. Vol. 355. Núm. 2. 2009. Pag. 109-113
http://dx.doi.org/10.1016/j.jnoncrysol.2008.10.017

Figure 4

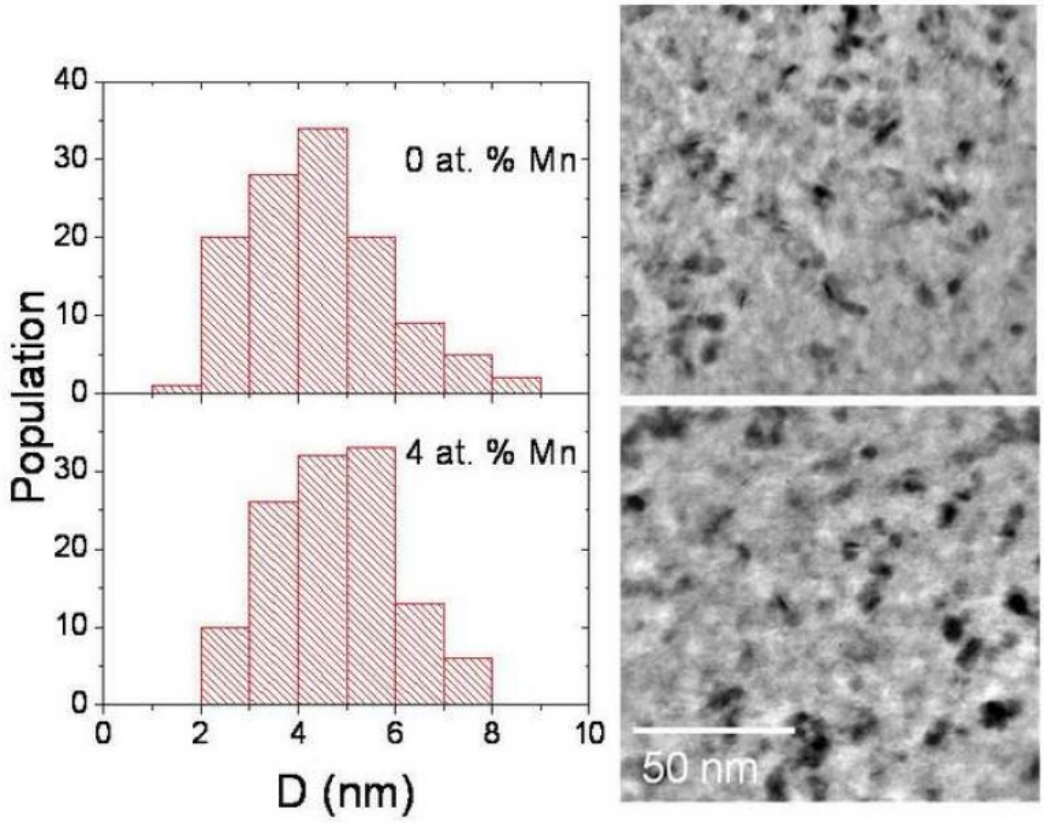

Journal of Non Crystalline Solids. Vol. 355. Núm. 2. 2009. Pag. 109-113
http://dx.doi.org/10.1016/j.jnoncrysol.2008.10.017

Figure 5

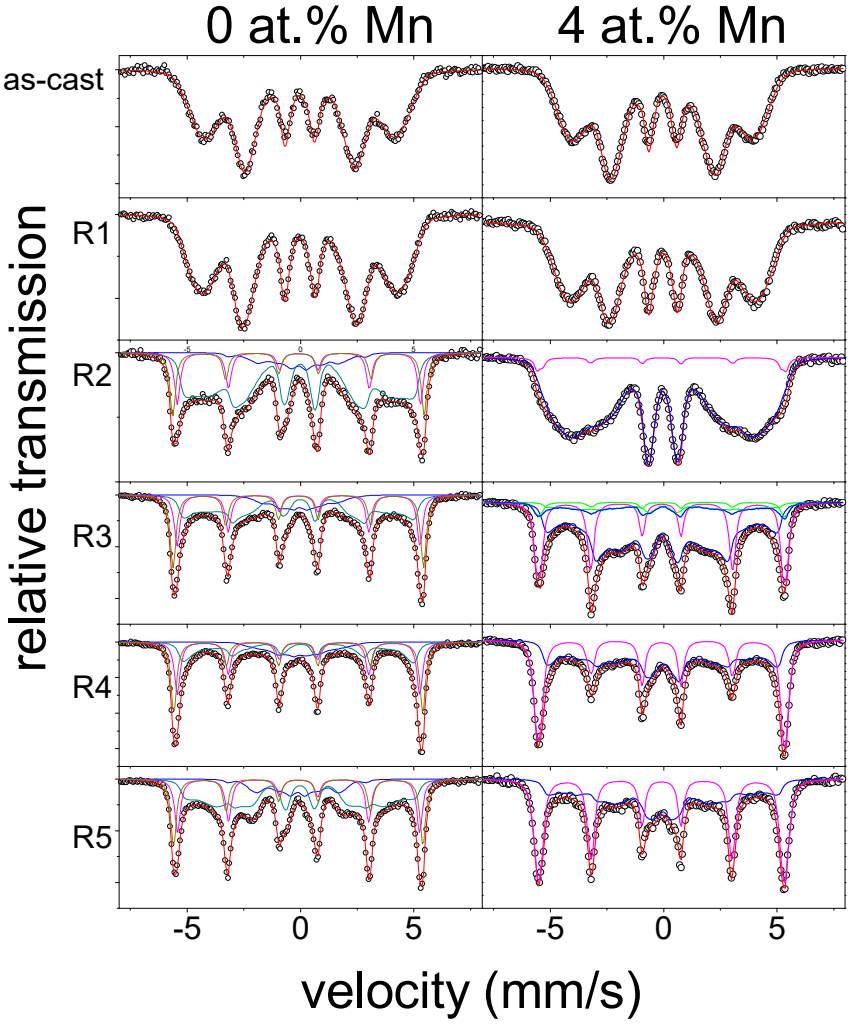

Journal of Non Crystalline Solids. Vol. 355. Núm. 2. 2009. Pag. 109-113
http://dx.doi.org/10.1016/j.jnoncrysol.2008.10.017

Figure 6

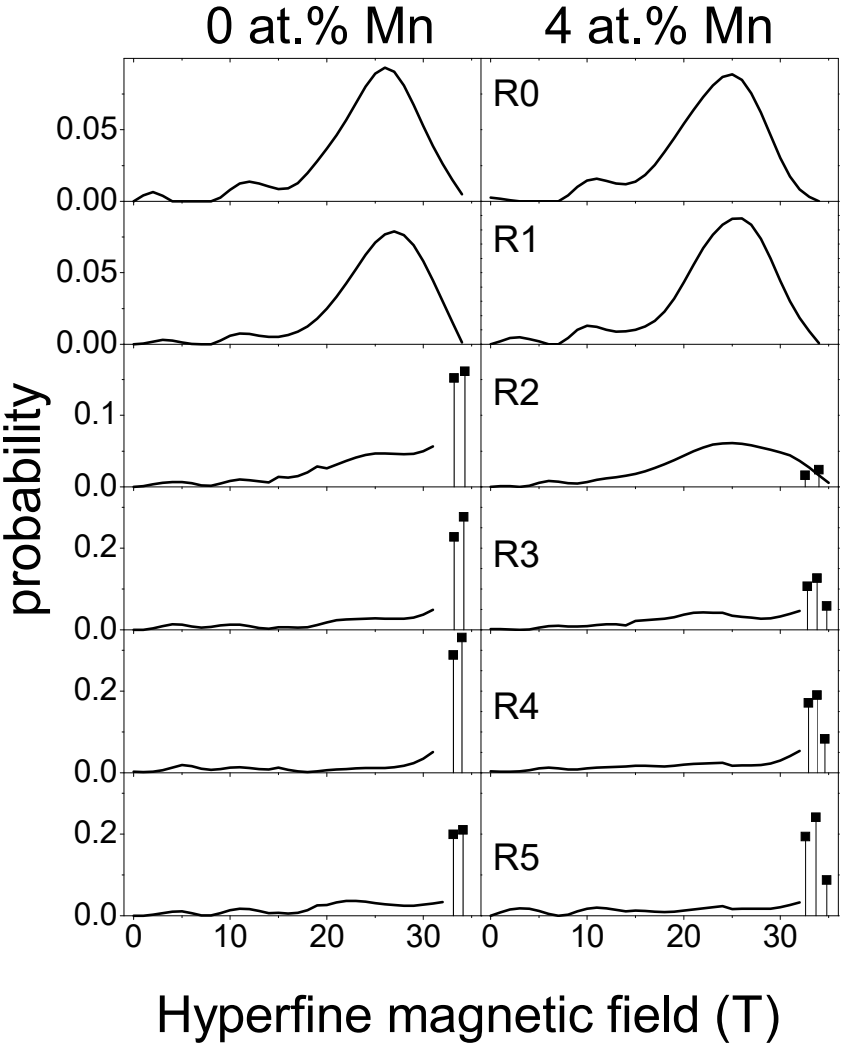

Journal of Non Crystalline Solids. Vol. 355. Núm. 2. 2009. Pag. 109-113
http://dx.doi.org/10.1016/j.jnoncrysol.2008.10.017

Figure 7

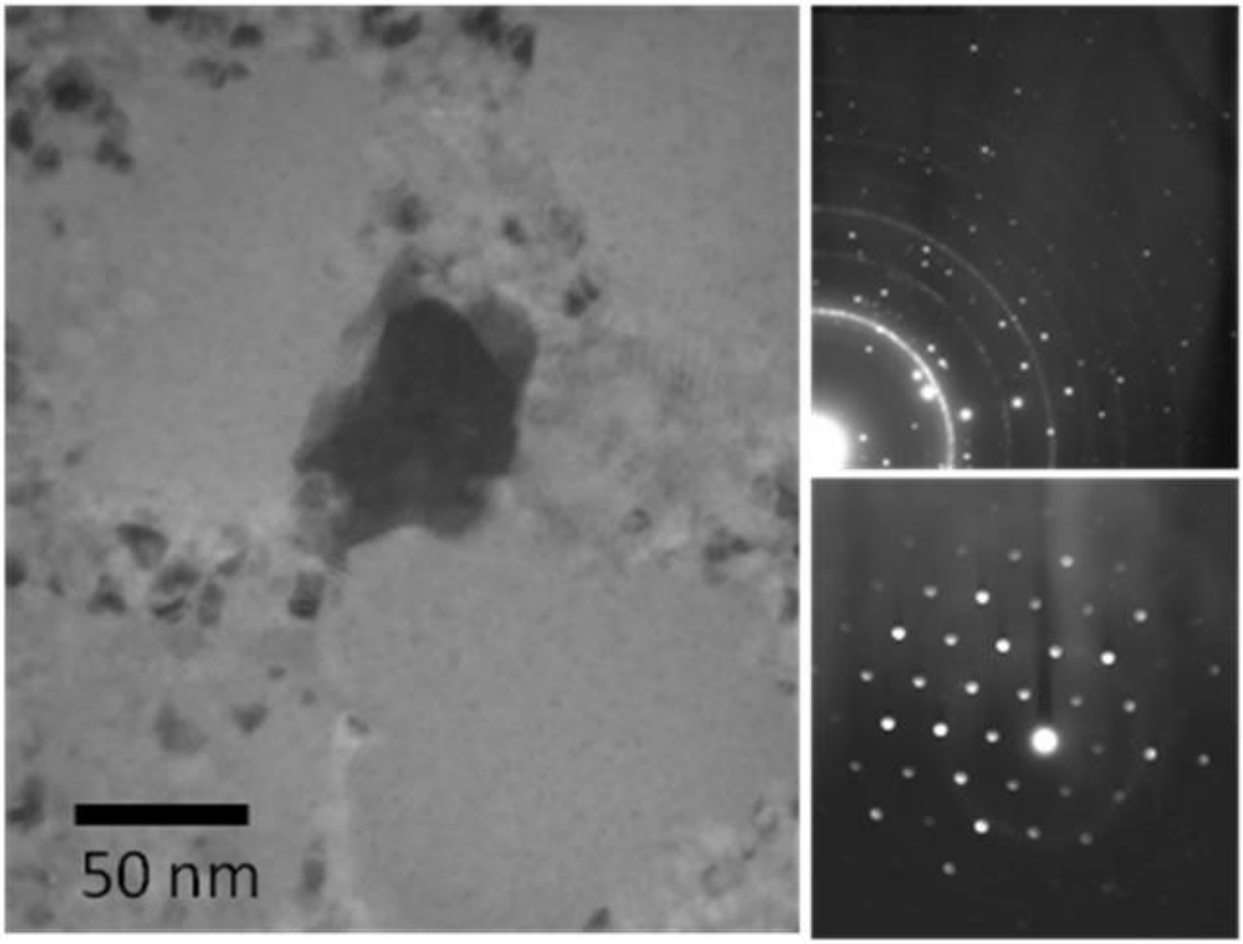

Journal of Non Crystalline Solids. Vol. 355. Núm. 2. 2009. Pag. 109-113
http://dx.doi.org/10.1016/j.jnoncrysol.2008.10.017

Referencias

[1] Y. Yoshizawa, S. Oguma, K. Yamahuchi, J. Appl. Phys. 64 (1988) 6044.
[2] M.E. McHenry, M.A. Willard, D.E. Laughlin, Progress in Mater. Sci. 44 (1999) 291.
[3] R.S. Sundar, S.C. Deevi, Int. Mater. Rev. 50 (2005) 157.
[4] A. Hernando, M. Vázquez, T. Kulik, C. Prados, Phys. Rev. B 51 (1995) 3581.
[5] K. Hono, Progress in Mater. Sci. 47 (2002) 621.
[6] J.S. Blázquez, V. Franco, A. Conde, J. Phys.: Cond. Matter 14 (2002) 11717.
[7] J.S. Blázquez, V. Franco, C.F. Conde, A. Conde, J. Magn. Magn. Mat. 254-255 (2003) 460.
[8] Y. Zhang, J.S. Blázquez, A. Conde, P.J. Warren, A. Cerezo, Mater. Sci. Eng. A 353 (2003) 158
[9] D.H. Ping, Y.Q. Wu, K. Hono, M.A. Willard, M.E. McHenry, D.E. Laughlin, Scripta Mater. 45 (2001) 781
[10] R.A. Brand, J. Lauer and D.M. Herlach, J. Phys. F: Met. Phys. 12 (1983) 675
[11] J.S. Blázquez, C.F. Conde, A. Conde, J. Non-Cryst. Solids, 287 (2001) 187
[12] J.S. Blázquez, C.F. Conde, A. Conde, Appl. Phys. Letters 79 (2001) 2898.
[13] T.B. Massalski, H. Okamoto, P.R. Subramanian, L Kacprzak, in “Binary Alloys Phase Diagrams”, (ASM International, Materials Park, Ohio, 1992)
[14] H. Okamoto, H. Okamoto (Ed.), Fe-Mn (Iron-Manganese) in Phase Diagrams of Binary Iron Alloys, ASM international, Materials Park, 1993.
[15] R.M. Bozorth, in “Ferromagnetism” (Van Nostrand, Princeton, NJ, 1968) p. 192
[16] C.F. Conde, A. Conde, P. Svec and P. Ochin, Mat. Sci. Eng. A 375-377 (2004) 718.
[17] H. Benaini, J.S. Blázquez, C.F. Conde, A. Conde, J. All. Comp. 454 (2008) 156.
[18] H.E. Kissinger, Anal. Chem. 29 (1957) 1702
[19] J.S. Blázquez, C.F. Conde, A. Conde, Acta Mater. 53 (2005) 2305.
[20] J.S. Blázquez, M. Millán, C.F. Conde, A. Conde, Phil. Mag. 87 (2007) 4151.
[21] J.S. Blázquez, V. Franco and A. Conde, J. Alloys Compd. 422 (2006) 32.
[22] H.H. Hamdeh, J. Okamoto, and B. Fultz, Phys. Rev. B 42 (1990) 6694.
[23] J.S. Blázquez, A. Conde, J.M. Grenèche, J. Phys.: Cond. Matter 15 (2003) 7843.